applied optics

All-sky camera system providing high temporal resolution annual time series of irradiance in the Arctic

Geir Johnsen,[1,2,*] Artur Zolich,[1] Stephen Grant,[1] Rune Bjørgum,[1] Jonathan H. Cohen,[3] David McKee,[4,5] Tomasz P. Kopec,[4] Daniel Vogedes,[4] and Jørgen Berge[1,2,4]

[1]Centre for Autonomous Marine Operations and Systems, Department of Biology, Norwegian University of Science and Technology (NTNU), Trondheim Biological Station, NO-7491 Trondheim, Norway
[2]University Centre in Svalbard (UNIS), P.O. Box 156, NO-9171 Longyearbyen, Norway
[3]University of Delaware, School of Marine Science & Policy, 700 Pilottown Rd., Lewes, Delaware 19716, USA
[4]Faculty of Biosciences, Fisheries and Economics, UiT The Arctic University of Norway, NO-9037, Tromsø, Norway
[5]Physics Department, University of Strathclyde, Glasgow G4 0NG, Scotland, UK
*Corresponding author: geir.johnsen@ntnu.no

Received 15 March 2021; revised 26 May 2021; accepted 29 May 2021; posted 2 June 2021 (Doc. ID 424871); published 23 July 2021

The ArcLight observatory provides hourly continuous time series of light regime data (intensity, spectral composition, and photoperiod) from the Arctic, Svalbard at 79° N. Until now, no complete annual time series of biologically relevant light has been provided from the high Arctic due to insufficient sensitivity of commercial light sensors during the Polar Night. We describe a camera system providing all-sky images and the corresponding integrated spectral irradiance (E_{PAR}) in energy or quanta units, throughout a complete annual cycle. We present hourly–diel–annual dynamics from 2017 to 2020 of irradiance and its relation to weather conditions, sun and moon trajectories.

https://doi.org/10.1364/AO.424871

1. INTRODUCTION

Continuous annual monitoring of light climate in the Arctic, relevant for terrestrial and marine biological processes and ecosystems, has never previously been recorded. The main reason for this is that the light intensity during the Polar Night is below the detection limit of commercially available light sensors. North of the Arctic Circle (66.3°N), the seasonal variation in the light climate (irradiance, spectral irradiance, and photoperiod) is highly dynamic throughout the year [1,2]. This seasonal variation increases with latitude, mostly due to increased darkness during the Polar Night [3]. During summertime in the polar region, the sun stays above the horizon for a minimum of one 24 h cycle called a Polar Day. At 79°N, the latitude of Ny-Ålesund ArcLight observatory (Fig. 1) described in this paper, the Midnight Sun period lasts from 18 April through 24 August [4]. Correspondingly, during the Polar Night, the sun is below the horizon for at least one 24 h cycle. At 79°N, the Polar Night lasts from 25 October through 17 February. For definitions of Midnight Sun and Polar Night, defined by solar elevation, see [1]. As the latitude increases, these periods of Polar Day or Polar Night are extended, ultimately with only one sunrise and one sunset over the entire year at the North Pole (latitude 90°N). The extent of Polar Night increases and the intensity of solar radiation decreases in a transect from the Arctic Circle to the North Pole [5,6].

The Polar Night can be considered as an annual process, divided into four different light-level zones, defined by the angle of the sun with respect to the horizon [1]. However, the solar elevation is constantly changing throughout the 24 h cycle in each of these four zones, whether the sun is visible or not. At a given location, the exact level of the Polar Night light climate depends not only on latitude, but has a temporal component as well.

Although the sun remains below the horizon during the entire diel cycle during the Polar Night, irradiance from the sun is still present as diffuse atmospheric light with a variation in intensity over the 24 h cycle. In addition, the Polar Night light climate is affected by lunar illumination, especially during periods of the Polar Night when the absolute levels of lunar light exceed that of sunlight [7]. The light climate is further affected by illumination from the *aurora borealis*. All three of these light sources change in intensity during a diel cycle. Consequently,

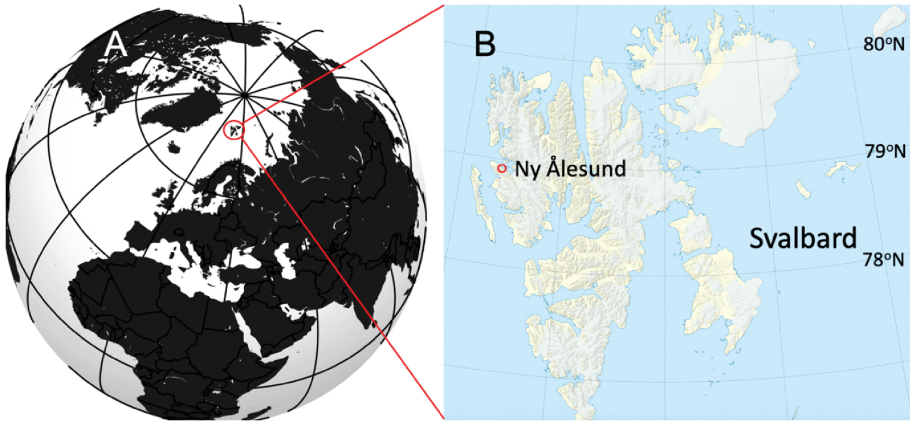

Fig. 1. (a) Location of Svalbard (red circle). (b) Position of the ArcLight light observatory west of Ny Ålesund (red circle) in Kongsfjorden, Spitsbergen (major island of the Svalbard archipelago). Source: Wikimedia Commons, A S. Solberg, Aquarius.geomar.de, CC by SA 3.0 (https://commons.wikimedia.org/w/index.php?curid=5644940). B E. Gaba by CC SA 4.0.

the observed heterogeneous light climate has been documented to be an important cue for marine organisms during the Polar Night period [5,8,9,10,11,12].

Irrespective of the geographical location, the light climate can be described by three key components: intensity (irradiance, E), spectral composition (E(λ)), and photoperiod (also called daylength or photophase). Irradiance is commonly measured in energy ($W\,m^{-2}$) or in quanta ($\mu mol\,m^{-2}\,s^{-1}$) units. For biological applications, E is usually measured in the spectrally integrated visible range (400–700 nm, or photosynthetic active radiation, PAR) hereby defined as E_{PAR}. The dynamics of the light are highly dependent on solar angle, but also on local weather, such as cloud cover, precipitation, snow conditions, and celestial dynamics such as lunar cycle and *aurora borealis*. Documentation of temporal changes in the light climate is relevant for application in models estimating start and end of ecophysiological responses such as phytoplankton blooms, determining growth periods of marine photosynthetic micro- and macro algae, and how the light climate is a cue for behavior in terrestrial higher plants, mammals, zooplankton, and fish [11,12].

The duration of E_{PAR} above a given light intensity (defined by the ability to detect light by a given organism or sensor of interest), during the diel light cycle at a given location, defines the photoperiod. Periods when E_{PAR} below that given intensity can be denoted as "night" or scotophase, e.g., when E_{PAR} is too low to induce a biological response, such as diel vertical migration (DVM) of zooplankton [11] or a photosynthetic event [12]. For some biophysical–chemical processes, the Polar Day represents the active period characterized with light intensities above threshold level for a given activity such as photosynthesis. On the other hand, during the Polar Night, characterized by low E_{PAR}, there is still enough light available to act as a cue for organisms such as DVM of zooplankton [5,13–15]. The definition of "day" and "night" is therefore organism dependent and needs to take into account overall light level, spectral light quality, and spectral sensitivity of the organism.

Recent publications have documented that during the darkest part of the Polar Night, when diffuse sky illumination from the sun is low compared to the major contribution from lunar

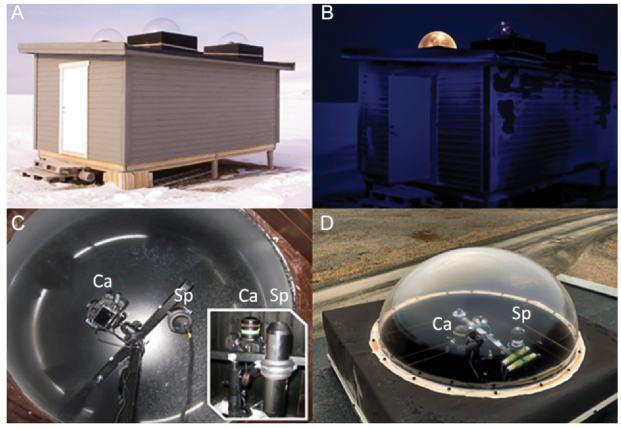

Fig. 2. (a) ArcLight observatory (b) in Polar Night with 1 of 4 domes illuminated for illustration purposes. (c) Camera (Ca) and spectroradiometer (Sp) with apertures pointing upwards through plexiglass dome. Insert shows all-sky camera and spectroradiometer. (d) Sensors viewed from outside the dome.

illumination, the latter provides the primary environmental cue for marine organisms [7,11,14]. The established perception of the Arctic region has been an ecosystem that enters a period of inactivity during the Polar Night [5]. Today it is documented that the ecosystem is in full operation, and that light is the major driver of biological processes even during the darkest part of the Polar Night [6–8,13,14]. Hence, there is a motivation to be able to quantify the biologically relevant light climate throughout the entire year, including the Polar Night. The light observatory (Fig. 2) was established as a part of the "Applied technology, biological interactions and consequences in an era of abrupt climate change" infrastructure project funded by the Norwegian Research Council. The goal was to provide new and quantitative information of light regime dynamics at different temporal perspectives ranging from annual, seasonal, monthly, and weekly to diel and hourly changes.

In this paper, we present a new methodology to extract quantitative complete annual time series measurements using all-sky images to identify sun and moon trajectories, aurora, clouds, precipitation, artificial light, and the corresponding E_{PAR} using

a high sensitivity camera placed in a light observatory at 79°N in Spitsbergen. In addition, a spectroradiometer is used for comparison and verification purposes. Step-by-step procedures and the algorithms used to determine E_{PAR} using the RGB channels of the camera are presented.

2. MATERIAL AND METHODS

The light observatory (hereafter *ArcLight*) is located close to The Norwegian Mapping Authority's Geodetic Earth Observatory station at Brandalspynten, situated about 4 km west of Ny-Ålesund settlement, Spitsbergen (78.9°N, 11.9°E, Fig. 1). The distance from Ny-Ålesund limits the impact from artificial light sources. The cabin in which the ArcLight sensors are mounted is heated and has an internet connection that enables communication with local control computers processing algorithms which run continuously (Fig. 2). A transparent plexiglass dome is fitted to the roof providing a 180° view of the atmosphere. A wavelength independent transmission coefficient for the dome was calculated by taking simultaneous spectroradiometer measurements using the USSIMO (details in Section 2.A) below the dome and a SpectraPen LM500 (PSI, Drasov, Czech Rep) irradiance sensor above the dome. All sensors in the observatory are positioned ~20 cm underneath the top of the dome and attached to a horizontal rod fitted to a tripod. Their apertures are facing upwards for measurements of downwelling E_{PAR} and spectral irradiance, $E(\lambda)$ [Fig. 2(d)]. The sensors can be remotely controlled to change settings and for data retrieval. The spectroradiometer measures hourly $E(\lambda)$ to provide E_{PAR} data in concert with the camera. Both sensors are connected to a dedicated computer running inside the cabin. The light climate data presented herein covers nearly four years of continuous measurements from 21 January 2017 to 1 November 2020 with 1 h temporal resolution. The sensors presented here are a spectroradiometer (Section 2.A) and an all-sky camera system (Section 2.B).

A. Spectroradiometer

The spectroradiometer is a hyperspectral USSIMO spectroradiometer (*In-situ* Marine Optics, Perth, WA, Australia) equipped with a Zeiss MMS1 UV-VIS NIR detector and National Institute of Standards and Technology (USA) traceable radiometric calibration between 380 and 900 nm. This instrument is used for time-series measurement of downwelling spectral irradiance in energy ($W\,m^{-2}\,nm^{-1}$) or quanta ($\mu mol\,m^{-2}\,s^{-1}\,nm^{-1}$) units for comparison and verification of E_{PAR} derived from the camera (Figs. 3 and 4). Spectral resolution is 10 nm (3.3 nm pixel spacing), and a cosine-corrected polytetrafluoroethylene (PTFE) light diffusor of 180° viewing angle with cosine error: <3% (0–60°), <10% (60°–87.5°) is fitted. The detection limit for the spectroradiometer is E_{PAR} of $0.016\,W\,m^{-2}$ (400–700 nm) based on the annual time series presented in Section 3. The device acquired measurements with a 16 bit analog to digital converter, with sampling rate up to 5 Hz and integration time from 1 to 6000 ms. This sensor is equipped with additional GPS, pitch, roll, heading, internal temperature, and depth sensors. The pitch and roll sensor is used to ensure that the spectroradiometer remains in a fixed position throughout the time-series acquisition.

Fig. 3. Illustration of camera CMOS light sensor: Red spot indicates area of pixels with active light capture of 180° viewing angle obtained from 8 mm fish-eye lens. Black area represents non-illuminated area of pixels, denoting dark current.

B. Camera Providing All-Sky Images and E_{PAR}

The all-sky camera is based on a Canon D5 Mark III EOS camera (Canon Inc., Tokyo, Japan) with a full-size CMOS sensor (36 × 24 mm, providing a crop factor of 1) and with 22.3 megapixel effective spatial resolution (Figs. 2 and 3). The camera is equipped with a fish-eye lens with a focal length set to 8 mm with aperture manually set to open (f/4) to ensure maximum sensitivity (Canon EF 8–15 mm f/4L), providing a 180° image of the atmosphere (only possible with a full-size sensor, Fig. 3). Both shutter speed (exposure time, ranging from 0.000125 to 30 s) and ISO (sensitivity, ranging from 100 at Midnight Sun period and up to 6400 during Polar Night, see key assumptions A–H below) are variable to obtain correct light exposure.

Note that these settings are far from detection limits and nonlinear responses (exposure time can be longer and the gain setting goes up to ISO of 25600, https://clarkvision.com/articles/evaluation-canon-5diii/). The camera system is calibrated to provide E_{PAR} in $W\,m^{-2}$ by using data from the red, green, and blue wavebands (RGB channels) for postprocessing. The camera is controlled using Canon EOS Utility software and a custom script to acquire images at user-specified times. Pictures acquired in RAW format are saved in a JPEG file format with quality: 97, subsampling ON (2 × 1). White balance was manually set to "daylight." Resolution of each image is 5760 × 3840 pixels with 24 bit per pixel color depth, distributed with 8 bits for each channel of red, green, and blue, giving RGB color space of the pictures according to the specifications [16]. All files are marked with an additional EXIF information set. Conversion of RGB images to E_{PAR} is described in detail in Section 2.C.

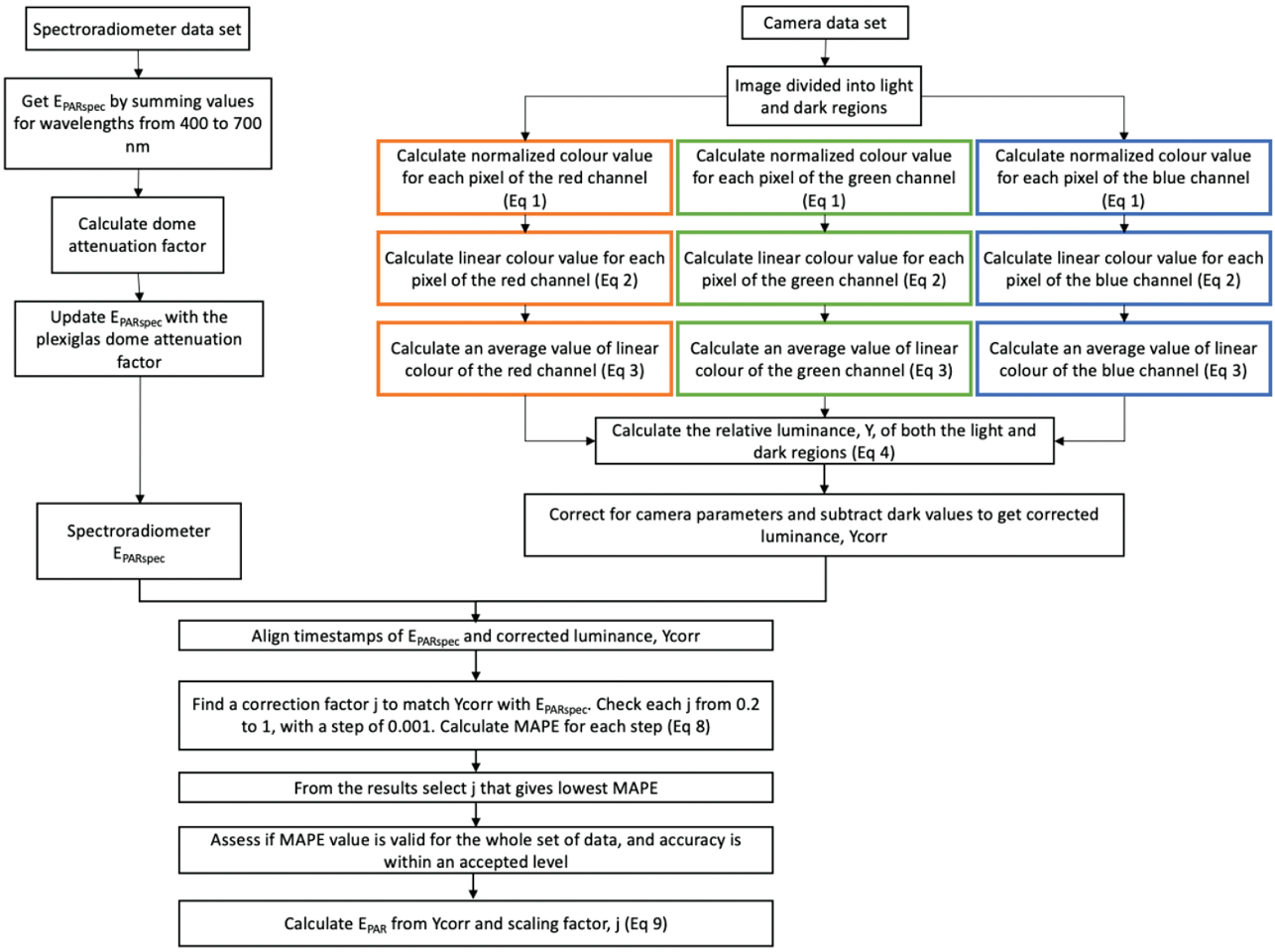

Fig. 4. ArcLight sensor flowchart showing processing and calculation steps for camera and spectroradiometer to provide E_{PAR}. MAPE denotes mean average percentage error [Eq. (8)] and j denotes a statistically derived scaling factor to transform calculated luminance values into irradiance values [Eqs. (7)–(9)].

C. Conversion of Camera Images to E_{PAR}

Several steps must be followed to obtain irradiance data from the camera. The camera data is in the form of pixel values in sRGB color space. These values must first be normalized using Eq. (1), the first step of the three colored sub-branches in the flow chart in Fig. 4:

$$C_s' = \left(\frac{C_{value}}{255}\right), \quad C \in \{R, G, B\}, \tag{1}$$

where C is used as a symbol representing a particular RGB color channel, C_s' is the normalized pixel value for that color channel (i.e., R_s' is the normalized pixel values for the red color channel, G_s' for the green channel, and B_s' for the blue channel), and C_{value} is the raw pixel value of the color channel. This normalized value is then linearized using Eq. (2) below, corresponding to the second step on the colored sub-branches ([16], Annex F, Eq. F4–7) detailed in Fig. 4:

$$C_s = \begin{cases} \left(\frac{C_s'}{12.92}\right), & 0 \le C_s' \le 0.04045 \\ \left(\frac{C_s'+0.055}{1+0.055}\right)^{2.4}, & 0.04045 < C_s' \le 1 \end{cases} \quad C \in \{R, B, G\}, \tag{2}$$

where C_s is the linear pixel value and C_s' is the normalized pixel value from Eq. (1). This value is then used to calculate the average value of the entire image for each color channel using Eq. (3), the final step on the colored sub-branches in Fig. 4:

$$\bar{C}_s = \frac{\sum_{i=1}^{pixels} C_s}{pixels}, \quad C \in \{R, B, G\}, \tag{3}$$

where $\bar{C}_s$ is the average linear value and pixels is the number of pixels contained in the area of interest of the image. The 8 mm "fisheye" view lens deployed gives a circular 180° image that fills approximately 52% of the camera CMOS detector. The remaining 48% should be completely black, with any measured signal representing noise. To calculate a correct color average, only the central, illuminated part of the images was considered in the analysis (Fig. 4). The dark signal was clearly below the illuminated part of the sensor throughout the seasons and will be detailed elsewhere. The lowest E_{PAR} from 22 December 2017 (winter solstice) at midnight was 1.98×10^{-6} W m^{-2} and 0.32×10^{-6} W m^{-2} for the illuminated area (red part of Fig. 3) and dark area indicating dark current (dark part of Fig. 3), respectively. This gave a signal to noise ratio of 6.12 at the most extreme low-light period during the four-year time series.

Prolonged exposure time or higher gain settings to enhance camera sensitivity were not needed during the extreme low-light periods.

The radius of the illuminated circle is 1920 pixels (Fig. 3). Using the calculated value for each color channel, the relative luminance, Y, in sRGB color space was calculated as follows [16] for both the light and dark regions:

$$Y = 0.2126 \cdot \bar{R}_s + 0.7152 \cdot \bar{G}_s + 0.0722 \cdot \bar{B}_s. \quad (4)$$

Several key assumptions have been made regarding generating quality radiometric data from the Canon imaging system:

A. The camera sets its parameters according to the exposure equation Eq. (5), defined in International Organization of Standardization (ISO) 2720:1974 standard [17] as

$$\frac{N^2}{t} = \frac{LS}{K}, \quad (5)$$

where N is the f-number (lens aperture), t is the exposure time (sec), S is the ISO (camera gain settings), L is the average scene luminance (cd m^{-2}), and K is a reflected-light meter calibration constant.

B. Camera pixel values are linear (or close to linear) with changing ISO under constant luminosity, exposure time, and aperture [18,19].

C. Camera pixel values are linear (or close to linear) with changing exposure time under constant luminosity, ISO, and aperture [18,19].

D. The aperture doesn't change throughout the entire time series [aperture is in 100% open position to optimize signal to noise ratio, i.e., equal to F value (focal ratio) of objective defined as ratio of focal length to the diameter of open aperture].

E. Average scene luminance, L, is a good approximation of average absolute luminance, Y':

$$L \approx Y'. \quad (6)$$

F. Absolute luminance, Y', depends on relative luminance Y measured by the camera and a scaling factor, j:

$$Y' = j \cdot Y. \quad (7)$$

G. The value recorded by each pixel of the recorded image can be transformed so it represents a value related linearly to the relative luminance, Y, as seen above.

H. Spectral response boundaries of the Canon 5D Mark III camera are similar to the photosynthetically active radiation (PAR, 400–700 nm) range [18].

I. The absolute luminance derived from the camera output, Y', is linearly proportional to E_{PAR}.

Based on these assumptions, the relative luminance, Y, from Eq. (4) is corrected for camera parameters to give a corrected luminance value. This is calculated for both the light and the dark pixel regions in each photograph giving Y_{Light} and Y_{Dark}, respectively, and is calculated using $Y_{\mathrm{Light\ or\ Dark}} = Y(N^2/St)$, where Y is calculated from the light or dark region, respectively. A dark-corrected, parameter-scaled luminance, $Y\mathrm{corr}$, is then obtained from $Y\mathrm{corr} = Y_{\mathrm{Light}} - Y_{\mathrm{Dark}}$.

The factor j from Eq. (7) can be found by minimising the mean average percentage error (MAPE) between the corrected absolute camera luminance, $Y\mathrm{corr}$, and the estimate of E_{PAR} obtained from the USSIMO spectroradiometer, E_{PARspec}, using

$$e = \frac{100\%}{n} \sum_{i=1}^{n} \left| \frac{E_{\mathrm{PARspec}} - Y\mathrm{corr} \cdot j}{E_{\mathrm{PARspec}}} \right|. \quad (8)$$

The MAPE, e, can be computed for each sample where E_{PARspec} was greater than the USSIMO detector limit (0.016 W m^{-2}, based on the time series presented in this paper, see Results section). The camera pictures and spectroradiometer data were not recorded at precisely the same time and thus needed to be synchronized. This was done using the MATLAB retime (xxx, 'hourly', 'linear') and synchronize (xxx, xxx, 'hourly', 'fillwithconstant') functions.

By minimizing this error factor, the variable j can be determined. This is a scaling factor which allows conversion from corrected luminance, $Y\mathrm{corr}$, to an approximation of E_{PAR} using Eq. (9). The analysis of factor j from Eq. (8) has shown that the minimum MAPE value of 28.88% was achieved for a scaling factor of $j = 0.624$. The conversion from camera derived luminance, $Y\mathrm{corr}$, to irradiance is then made using the relationship shown in Eq. (9) based on the assumptions just listed:

$$E_{\mathrm{PAR}} \approx Y\mathrm{corr} \cdot j. \quad (9)$$

An E_{PAR} in air conversion factor of 4.6 is herein used to convert W m^{-2} to µmol m^{-2} s^{-1} ([20], Appendix A, "Units", p. 569).

D. Control Computer

The software on board the computer in the ArcLight observatory provides several functions: (1) takes camera pictures at predefined times, (2) records spectroradiometer data at a predefined time interval, (3) sends housekeeping notifications via e-mail, (4) creates backup copies of the data locally and in the cloud, and (5) provides access to the computer via a remote desktop.

A flow chart for the camera and spectroradiometer regarding processing, calculations, and correction factors to final data sets is shown in Fig. 4.

3. RESULTS

An illustration of all-sky images providing information for different light-regime scenarios is shown in Fig. 5. With the time series providing hourly all-sky images, light climate variations can be seen due to many factors (e.g., cloud cover, sun angle, moon angle, aurora, precipitation, and light pollution). All-sky images give valuable information with respect to quality control (the plexiglass dome can be covered with rain, snow, ice, moisture, sitting birds etc.). We can detect the extent of cloud cover, which is especially important at times with low E_{PAR}, a period particularly sensitive to light pollution. Likewise, we can also see the effect of the sun, the moon, and the northern lights in the corresponding E_{PAR} data.

The camera sensor performance (all-sky images and use as a light sensor) are elucidated by providing E_{PAR} data from spring,

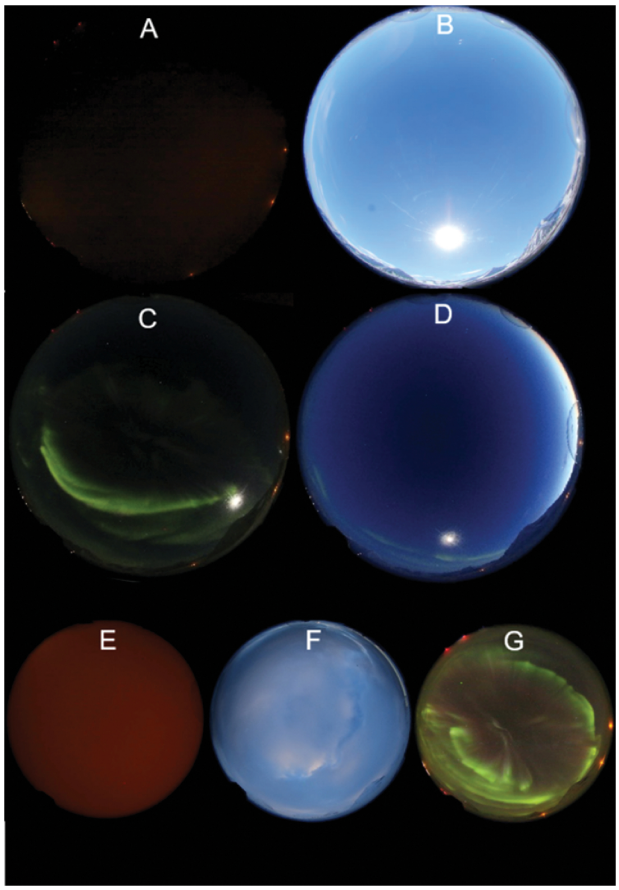

Fig. 5. All-sky images of 180° viewing angle (Canon 5D Mark III with 8 mm lens) from the ArcLight observatory showing different light field scenarios. (a) 22 December 2016, 12:00 (local noon) at the darkest time of year. (b) 21 June 2017, 12:00 (local noon, with the sun in south) at the brightest time of year. (c) 5 March 2017, 23:00 with moon illumination and northern lights. (d) 5 March 2017, 20:00 with clear sky and moon illumination. (e) 14 February 2017, 21:00 with light pollution; orange hue is from sodium street lights reflected by low cloud cover, with peak emission at 585 nm. (f) 5 March 2017, 15:00, sky with partial cloud cover. (g) 31 December 2016, 18:00, showing New Year's Eve with northern light.

summer (Fig. 6), and Polar Night (Fig. 7). Figure 6(a) shows all-sky images for a typical day in March 2017. During this 24 h period, the light climate transitions from nighttime darkness to bright sky and back, with the moon visible from 19:00 onwards. The E_{PAR} values can be seen to be in good agreement between both sensors in this case. The USSIMO spectroradiometer has a much higher dark current level than the camera leading to lower sensitivity, illustrated by the camera producing lower values of E_{PAR} when light intensities were below the spectroradiometer's measurement threshold of 0.016 W m^{-2}. The average daylight E_{PAR} values between 08:00 and 17:00 were measured as 10.53 W m^{-2} from the camera and 10.54 W m^{-2} from the spectroradiometer. The average nighttime values between 00:00–04:00 and 21:00–00:00 were measured as 1.07×10^{-5} and 5.95×10^{-3} W m^{-2} from the camera and spectroradiometer, respectively.

A 24 h time series during the Midnight Sun period [1 June 2017, Fig. 6(b)], with the sun visible at all times of the day, led to

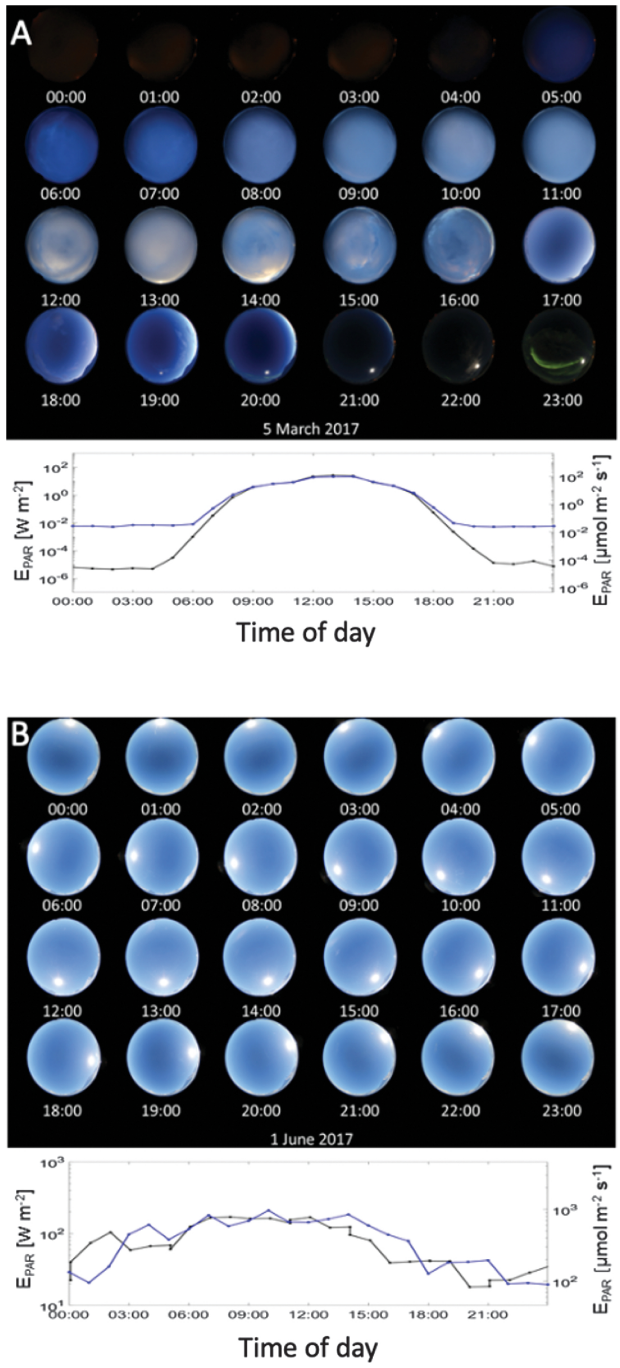

Fig. 6. Hourly all-sky images from 2017 captured during a full day in spring and summer period. (a) Spring time at 5 March, and (b) Midnight Sun period, 5 June. In (a), the detection limit of the spectroradiometer can clearly be seen during nighttime; also see that E_{PAR} from northern light is detectable at 23:00 by all-sky image and E_{PAR} camera. At 1 June (b), we see the 24 h trajectory of the sun, indicating a solar compass with the sun in the south at solar noon (12:00) and in the north at midnight (00:00). Lower panels denotes E_{PAR} on log-scale. Note scale differences on y axes. Blue and black lines indicates E_{PAR} from spectroradiometer and camera, respectively.

a consistently high E_{PAR} level, characterized by a low amplitude difference in E_{PAR} between day and night. Both sensors perform similarly in these light-rich conditions. Average E_{PAR} from the camera was 85.39 W m^{-2} during the 24 h period, while the

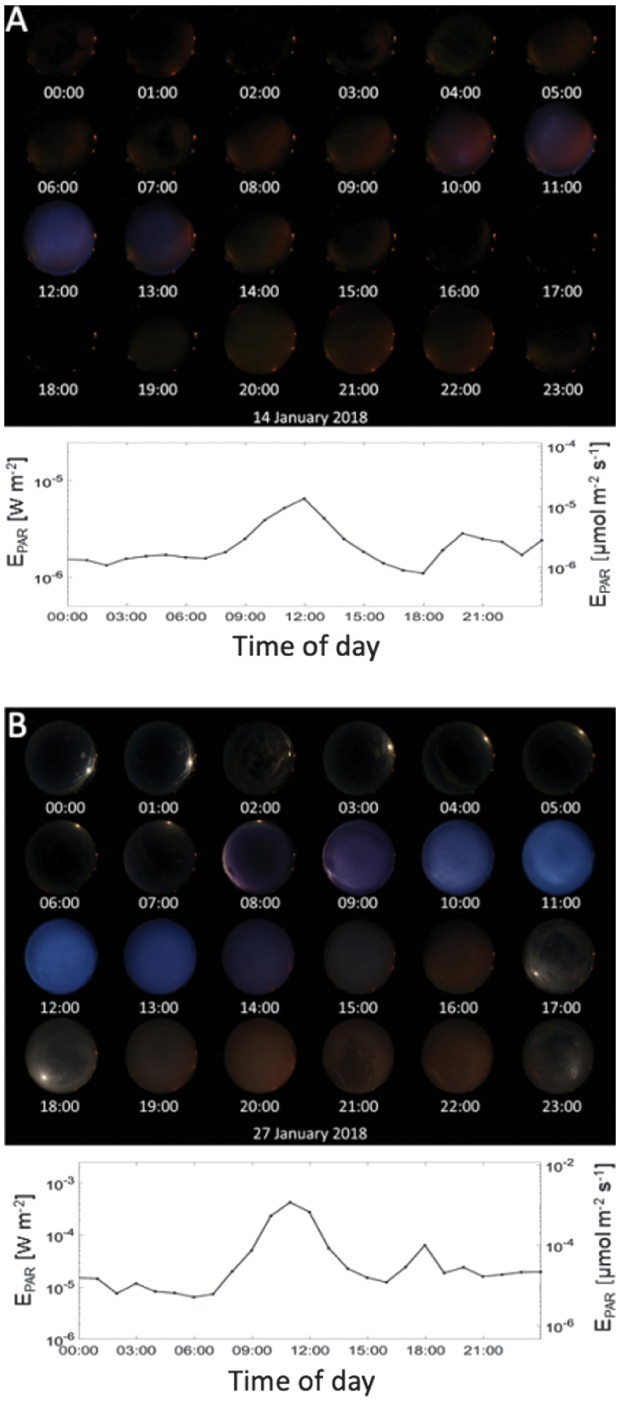

Fig. 7. Hourly all-sky images (upper panels) and E_{PAR} values (lower panels, y axis log scale) captured during the Polar Night in two days in January 2018. E_{PAR} from camera (black line). (a) 14 January 2018, indicating hourly differences in Polar Night E_{PAR} levels relative to (b) 27 January 2018 (13 days apart). In (b), the impact of moonlight is clearly seen from midnight to 08:00. Note scale differences on y axes.

spectroradiometer measured 94.45 W m^{-2}. The discrepancy when comparing the two sensors regarding E_{PAR} measurements in low- and high-light conditions is further discussed in the next section and is mainly due to lower light sensitivity of the spectroradiometer.

The differences in daily variation in E_{PAR} during and at the end of the Polar Night (14 and 27 January 2018) indicates the fast transition from extreme low light conditions to brighter conditions only two weeks apart (Fig. 7). During this period, the overall E_{PAR} is low and is dominated by the moon as the major illuminator and a brief period of increased diffuse solar illumination around solar noon. The E_{PAR} from northern lights and the effect of light pollution (reflected light from low hanging cloud cover from street lights from Ny-Ålesund, 4 km away) are also detected at 19:00–22:00 27 January 2018 [Fig. 7(b)]. This light pollution gave the all- sky images an orange hue [Fig. 5(e)] due to emission of sodium street lights from Ny Ålesund settlement, characterized by high spectral irradiance in the orange part (peak $\approx$ 585 nm) of the visible spectrum, detected by a high-sensitivity Ocean Insight QEPro spectrometer (data not shown). Figure 7(a) illustrates a clear night when the moon is not visible and impacts of light pollution and aurora are at a minimum. Here, the superior light sensitivity of the camera is far from the detection limits compared to the spectroradiometer, which was not able to detect these low light levels. Across this 24 h period, the camera measured an E_{PAR} of 2.35×10^{-6} W m^{-2}. Conversely, the data collected on 27 January 2017 (at the end of Polar Night season), when the moon was visible and light pollution was reflected from cloud cover, showed an order of magnitude increase in measured E_{PAR} [Fig. 7(b)]. The average E_{PAR} values obtained from the camera for this 24 h period were 5.51×10^{-5} W m^{-2}.

The full four-year hourly time series of E_{PAR} (in energy and quantum units) from January 2017 to November 2020 is presented in Fig. 8. The spectroradiometer E_{PAR} values are in agreement with the camera for $E_{PAR} > 0.016$ W m^{-2} (0.074 µmol m^{-2} s^{-1}), the detection limit of the spectroradiometer (Fig. 6). The resulting value of j [Eq. (9)] can be applied to camera data at low light levels below the sensitivity threshold of the spectroradiometer, allowing us to greatly extend the range of E_{PAR} observations. This difference in sensitivity is a major advantage of using the camera for low-light conditions such as the Polar Night with monthly average E_{PAR} ranging from 15×10^{-6} W m^{-2} in December (2017–2020) to 56×10^{-6} W m^{-2} in January 2018 and 2020 (Table 1). There is consistently good agreement between the sensors above the detection limit of the spectroradiometer [Fig. 6(b)].

Below 0.002 W m^{-2}, the camera was used to detect E_{PAR} which corresponded to the lunar trajectory cycle in twilight periods around spring and autumn equinoxes, and during Polar Night (detailed in Fig. 8). The E_{PAR} from the lunar illumination can be seen in Fig. 9, showing E_{PAR} as a function of percentage of moon disc illumination and sun angle. The E_{PAR} values are consistent in absolute irradiance for each new moon to full moon cycle, with the range is typically varying from 1×10^{-6} W m^{-2} at new moon to 320×10^{-6} W m^{-2} at full moon.

4. DISCUSSION

The expected maximum cosine-corrected surface noon downwelling E_{PAR} on a clear midsummer day in Ny-Ålesund should reach 1200−1400 µmol m^{-2} s^{-1} [2,21]. This is in agreement with our observations using both sensors. The recorded E_{PAR} from the ArcLight observatory during dark Polar Night is also

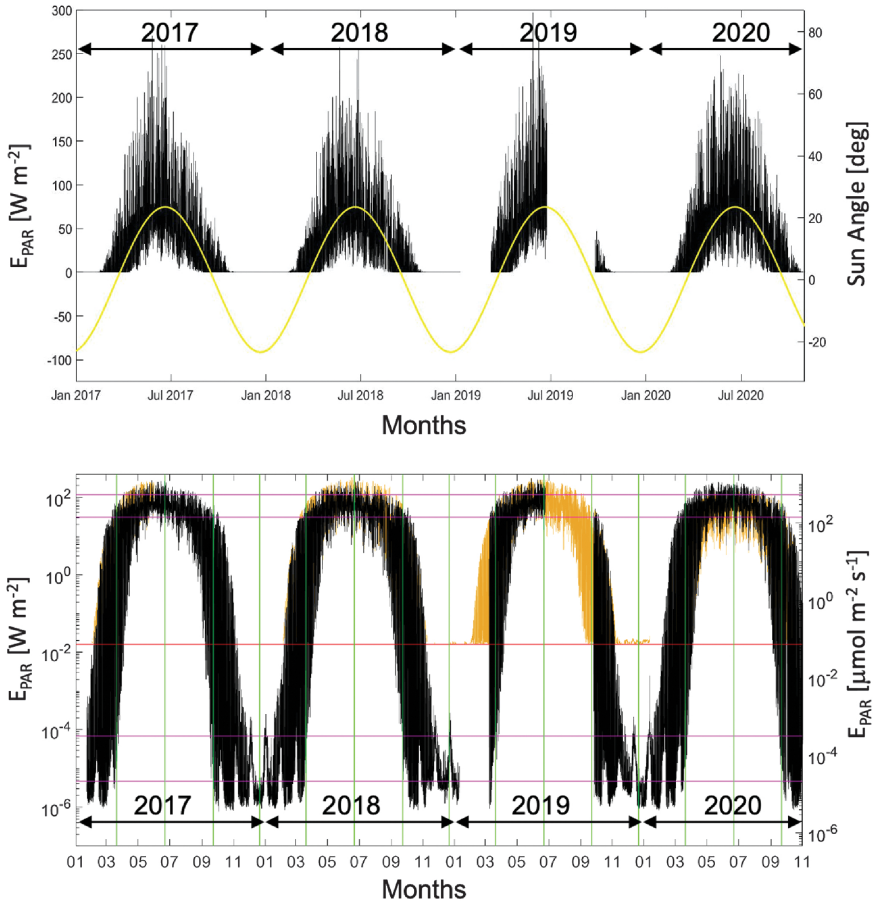

Fig. 8. Annual time series of E_{PAR} from the ArcLight observatory from 21 January 2017 to 1 November 2020 with a temporal resolution of 1 h. Upper panel: E_{PAR} from camera (linear scale, W m^{-2}) with corresponding sun angle (degrees, secondary y axis, yellow line). Lower panel: E_{PAR} (log-scale, primary y axis W m^{-2}, secondary y axis µmol m^{-2} s^{-1}). E_{PAR} values between camera (black lines) are in agreement with spectroradiometer data above spectroradiometer sensitivity threshold (orange line) of 0.016 W m^{-2}. Equinox (20 March and 22 September) and solstice (21 June and 21 December) are indicated by green vertical lines. Pink horizontal lines indicate average maximum (noon) and minimum (midnight) E_{PAR} (see text for details) during Midnight Sun (two upper lines) and Polar Night periods (two lower lines), respectively.

Table 1. Calculated % of Hours Per Month (H%) from 2017–2020 with E_{PAR} > 0.0022 W m^{-2} (0.01 µmol m^{-2} s^{-1}) Derived from Camera as Threshold for Actinic (Photosynthetic) Activity[a]

	2017	2018	2019	2020	2017	2018	2019	2020	2017–2020	
Month	H%	H%	H%	H%	Average E_{PAR} (W m^{-2})	Average E_{PAR} (W m^{-2})	Average E_{PAR} (W m^{-2})	Average E_{PAR} (W m^{-2})	Average E_{PAR} (W m^{-2})	
Jan	3.3[b]	0.1	0.0[b]	0.1	219.4E-06[b]	59.50E-06	3.33E-06[b]	50.96E-06	55.23E-06	±4.26E-06
Feb	31.2	29.5	—	30.6	0.58	0.31	—	0.59	0.49	±0.13
Mar	66.6	68.5	71.9[b]	67.9	11.44	11.00	13.95[b]	14.18	12.21	±1.41
Apr	100.0	100.0	100.0	100.0	40.50	38.85	36.95	47.30	40.90	±3.90
May	100.0	100.0[b]	100.0	100.0	73.10	69.37[b]	75.58	76.93	75.20	±1.59
Jun	100.0	100.0	100.0[b]	100.0	79.61	72.13	94.96[b]	85.15	78.96	±5.33
Jul	100.0	100.0	—	100.0	55.88	51.24	—	73.35	60.16	±9.52
Aug	100.0	100.0	—	100.0	38.06	41.11	—	45.83	41.66	±3.20
Sep	83.4	85.2	65.4[b]	82.3	12.68	16.04	8.41[b]	16.05	14.93	±1.59
Oct	42.3	44.4	44.0	42.9	2.09	2.55	1.90	1.44	1.99	±0.40
Nov	5.8	6.9	5.7	41.2[b]	1121E-06	2025E-06	1599E-06	26177E-06[b]	1582E-06	±368E-06
Dec	0.0	0.0	0.0	—	15.38E-06	15.69E-06	14.56E-06	—	15.21E-06	±0.48E-06

[a]Average E_{PAR} denotes the average monthly irradiance, ± denotes standard error (SE).
[b]Denotes partially missing data, — denotes entire month of missing data. These entries have not been used for average calculations for 2017–2020.

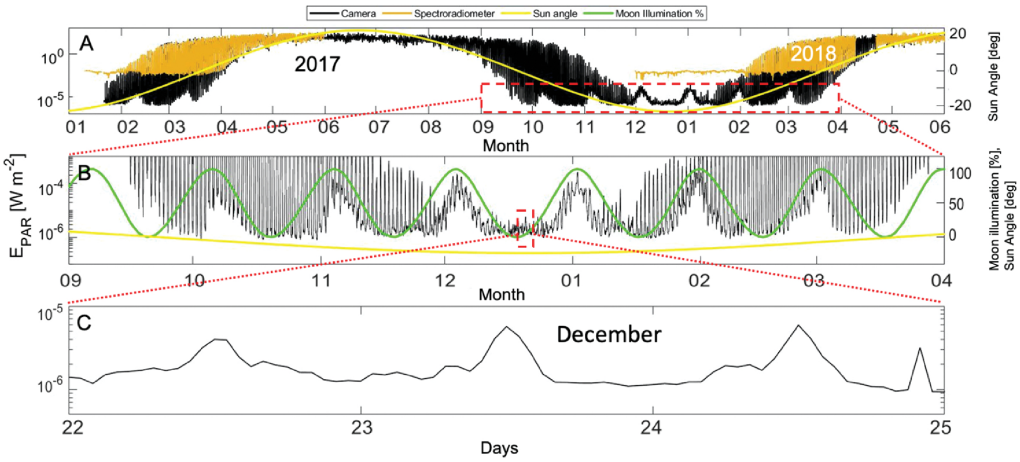

Fig. 9. Annual, monthly, and daily variation in 2017–2018 of E_{PAR} from the ArcLight observatory (all panels, y axes in log scale). (a) E_{PAR} from camera (black line) and orange line indicates spectroradiometer data. Sun angle (yellow) is shown on the secondary y axis. (b) E_{PAR} data from camera during the low-light period (Sep 2017–April 2018, red square in panel A, including Polar Night). E_{PAR} shows the prominence of moonlight as the main source of illumination, with peaks denoting full moon and minimum denoting new moon (green lines). The percentage of the moon's surface illuminated and the maximum daily sun angle are also shown on the second y axis. (c) E_{PAR} from darkest time of year (22–25 December), red square in B showing diel E_{PAR} changes. E_{PAR} closely follows the sun angle in bright season, in contrast to the low light season where the moon is the major illuminator. Low light season E_{PAR} measurements are sensitive to lunar cycle, light pollution, and snow on ground reflecting light to clouds.

in agreement with point measurements from the Kongsfjorden region in January 2014–2018 [1,8,14].

Light climate during the Polar Night can be further discussed by examining the long term, four-year period of light levels (Fig. 8), and it becomes clear that the moon is an important "illuminator" during the Polar Night [1,4], being an important cue for DVM of zooplankton [7]. As shown in Fig. 9, the annual cycle of irradiance levels is generally directly correlated to sun angle. However, during periods when the sun is below the horizon, the moon dominates as the ambient light source. The E_{PAR} peaks from October–March (2017–18) have a period of 29.5 days and correspond to the percentage of the moon's face which is illuminated. The moon moves through the same path in the sky as the sun during the annual cycle, meaning that the moon in midwinter will have the same elevation as the midday sun in midsummer.

During the Polar Night, the moon will be above the horizon for several days around the full moon period, and correspondingly, below the horizon for several days around a new moon. This means that the full moon during Polar Night imitates the elevation path of the sun during the Midnight Sun period. This sensitivity to the extent of the moon's face which is illuminated can be seen from measurements taken during the dark Polar Night (Fig. 9B). Our annual minimum E_{PAR} values between November and January ranged from $0.89-1.15 \times 10^{-6}$ W m^{-2}, while maximum E_{PAR} values were in the range of $221-413 \times 10^{-6}$ W m^{-2} (Figs. 8 and 9, Table 2), indicating a value of high-resolution time series that is highly dynamic and sensitive to time and latitude. Previous recorded values [7] include January 21, 2016, reported with scattered cloud conditions and an illuminated moon fraction of 89%, when E_{PAR} was estimated to be approximately 55×10^{-5} μmol m^{-2} s^{-1} or 12×10^{-6} W m^{-2} from a cruise to NW-Spitsbergen. Also, on January 21, 2014, with a small decrease in the illuminated moon fraction to 81%, a value of $10-15 \times 10^{-6}$ μmol m^{-2} s^{-1} or $2-3.3 \times 10^{-6}$ W m^{-2} was recorded [8]. Both of these are in good agreement with our data.

The terms "Midnight Sun period" and "Polar Night period" are defined by sun angle [1,4] and not light levels directly. However, based on our E_{PAR} time series, we can define the start and end of seasonal light periods based on absolute irradiance values and the effect on different organisms (see Table 1 and 2). Here, we define the duration of different "high-light periods" and "low-light periods" based on a coefficient of variation (CV) value that is calculated for each 24 h period to determine the amount of E_{PAR} variation per day. The coefficient of variation was calculated as a ratio of the standard deviation to the mean of E_{PAR} for a 24 h period. From this data, a typical day during the Midnight Sun period was characterized as having a CV value of 0.554 (55.4%) or less by taking the average of the CV value for a number of cloudless days around the summer solstice. This criterion was then used to approximate the beginning and end of E_{PAR}-defined "Midnight Sun" and "Polar Night" periods (Table 1 and 2). The same logic was applied to determine the approximate beginning and end of the E_{PAR}-defined Polar Night period; however, due to the larger level of variation and the effects of the full moon at the beginning and end of the Polar Night, the selection criteria needed to be different. Dates where the CV value fell below 1 and were not previously identified as being part of the Midnight Sun period were identified as Polar Night dates. The Polar Night dates determined in this manner are 29 November to 15 January in 2017/18, 18 November to 9 January in 2018/19 (note that there was missing data in January 2019), and 22 November to 19 January in 2019/2020. This gave us shorter Polar Night periods than the solar angle-based definition in [4] running from 25 October to 17 February.

Irradiance >0.002 W m^{-2} (>0.01 μmol m^{-2} s^{-1}) was detected from February to November in all years and didn't fall below this level at any point between late March and early

Table 2. Maximum and Minimum E_{PAR} (in Energy and Quanta) Defined "Midnight Sun Periods" (April–August) and "Polar Night" (November–January) 2017–2020 Derived from Camera[a,b]

		Max E_{PAR}		Min E_{PAR}	
Year	Period	W m^{-2}	μmol quanta m^{-2} s^{-1}	W m^{-2}	μmol quanta m^{-2} s^{-1}
2017	April–August	271	1247	2.10	9.66
	Nov–January	256E-06	1180E-06	0.94E-06	4.32E-06
2018	April–August	256	1178	1.10	5.06
	Nov–January	413E-06	1900E-06	1.15E-06	5.29E-06
2019	April–June[c]	304	1398	1.40	6.44
	Nov–January	221E-06	1330E-06	0.89E-06	4.09E-06
2020	April–August	247	1136	0.60	2.76
Average	April–August	270	1240	1.30	5.98
	Nov–January	319E-06	1468E-06	0.99E-06	4.55E-06

[a]Criteria for E_{PAR} characterizing Midnight Sun and Polar Night periods are given in text above.
[b]The annual E_{PAR} range and amplitude between daily maximum and minimum between Polar Night and Midnight Sun seasons are given in Fig. 11.
[c]Missing data from 24 June to September 2019 led to a shorter Midnight Sun period in 2019.

September. This is typical for the civil twilight period (sun elevation −6° to 0° below horizon). By using this threshold value as a guide, we can determine the photoperiod of organisms which respond at that light level, i.e., "daylight" indicates actinic $E_{PAR} > 0.01$ μmol m^{-2} s^{-1} for photosynthetic organisms. For example, for a week-long period in September 2018, the period where irradiance was above the threshold value is shown in Fig. 10. *In situ* observations of threshold level of E_{PAR} versus photosynthesis are sparse, and work from NE Greenland indicates a lower limit at 0.17 μmol m^{-2} s^{-1} (detection limit for E_{PAR} sensor in this study was 0.15 μmol m^{-2} s^{-1}) for sea-ice microalgae initial growth [22], see also discussions in [12,21]. Until now, commercial E_{PAR} sensors have limited photobiological research in finding lower threshold limits for actinic activities (land and sea), DVM, and the effects of light pollution. To make the "daylength" concept more physiologically and ecologically meaningful, we can utilize the E_{PAR} data in this study with corresponding spectral irradiance (data not shown) as input for the light sensitivity of the sensor (apparatus) or spectral response in a given organism such as using the *in vivo* Chl a-specific light absorption coefficient or fraction of absorbed light utilized by photosystem II for oxygen evolution (400–700 nm, m^2 mg Chl a^{-1}, detailed in [23,24]) to calculate the absorbed quanta in phytoplankton, which is the next step in further studies regarding photoperiod in an ecological context.

Seasonal differences in E_{PAR} can be further examined by using the estimated percentage of hours per month with E_{PAR} greater than a theoretical actinic limit (minimum light intensity to trigger a photosynthetic event) as an example indicating percentage of hours per month for potential photosynthetic activity (H%) from 2017–2020 with threshold $E_{PAR} > 0.0022$ W m^{-2} (0.01 μmol m^{-2} s^{-1}), Table 1. Based on this, H% is 0% in the darkest month (December), 0.1%–3% in January, 30% in February, 70% in March, 100% April–August (Midnight Sun period), 80% in September, 40% in October, and lastly, 6% in November (Table 1).

The monthly E_{PAR} averages are shown in Table 1 and range from 15×10^{-6} W m^{-2} in December (2017–2019) to 79 W m^{-2} in June (2017, 2018, and 2020). During the Midnight Sun period (2017–2020), the maximum E_{PAR} were found in April–August and ranged from 247−304 W m^{-2} (1136−1398 μmol m^{-2} s^{-1}, Table 2). In contrast, the minimum E_{PAR} during Polar Night, including November–January 2017–2019, ranged from $0.9-1.1 \times 10^{-6}$ W m^{-2} ($4.1-5.3 \times 10^{-6}$ μmol m^{-2} s^{-1}).

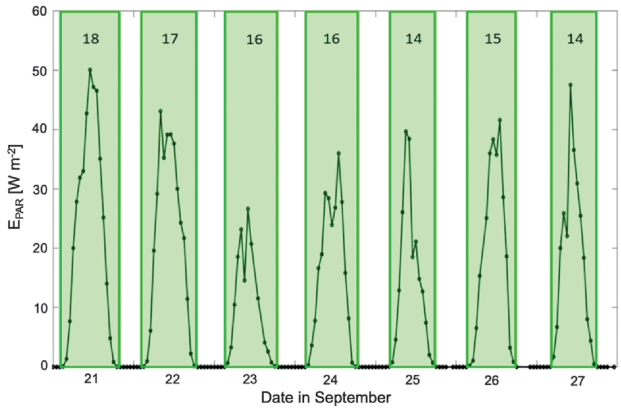

Fig. 10. Number of hours (on top of each green bar) per day during 2018 following autumn equinox 21 September period with $E_{PAR} > 0.002$ W m^{-2} (0.01 μmol m^{-2}s^{-1}) defined as limit for actinic activity and the corresponding daily decline in the photoperiod for photosynthetic active organisms.

By looking at the estimated % hours per month with E_{PAR} above 0.0022 W m^{-2} (0.01 μmol m^{-2} s^{-1}), H%, indicating the threshold of actinic light, we see that from April–August E_{PAR} is higher than 0.01 μmol m^{-2} s^{-1} at all times (i.e., H% of 100). In contrast, the Polar Night period has H% of 0% in December and close to 0.1 in January. The average E_{PAR} denotes the mean irradiance level per month and illustrates the fast transition of intensities in spring and autumn (Fig. 11).

From the four-year time series from 2017 to 2020 in Table 2, we see that the maximum average E_{PAR} in the Midnight Sun period from April–August (based on E_{PAR} data and the CV approach discussed previously to identify periods with similar intensities) is 270 W m^{-2} (1240 μmol m^{-2} s^{-1}). The corresponding minimum E_{PAR} was 207 times lower. In contrast, in the Polar Night period from November to January, the average maximum to minimum ratio of E_{PAR} was 322.

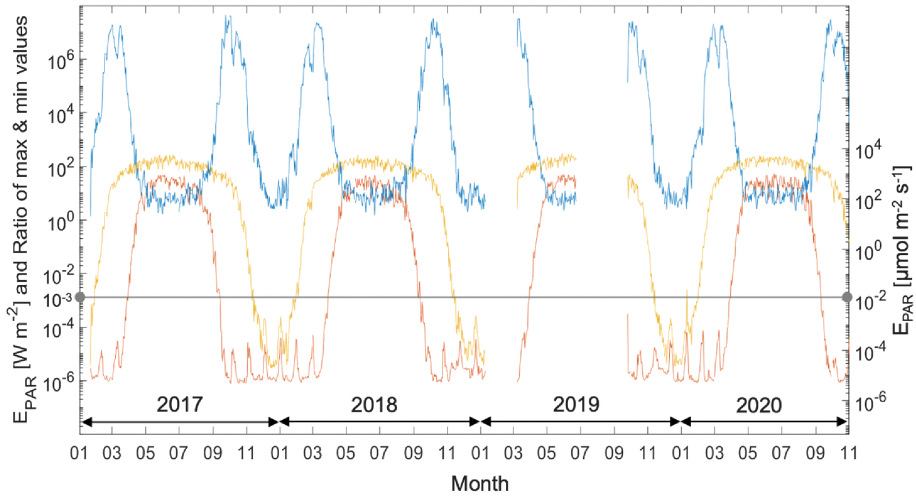

Fig. 11. Daily E_{PAR} from camera in the period 2017–2020 showing maximum E_{PAR} (orange line), minimum E_{PAR} (red lines), and corresponding maximum to minimum ratios (blue line) indicating daily amplitude variation as a function of seasons. Note the extremes of E_{PAR} amplitude during twilight periods in spring (months 3–4) and autumn (months 9–11), see Tables 1 and 2. Threshold E_{PAR} for actinic activity (photosynthesis) is set to 0.002 W m^{-2} (0.01 µmol m^{-2} s^{-1}) indicated by gray horizontal line.

This gave an E_{PAR}-defined Midnight Sun period from 22 April to 11 August in 2017, 20 April to 6 August in 2018, 21 April to 24 June in 2019 (this early end is due to missing data from 24 June to 25 September 2019), and 21 April to 25 August in 2020. This is in agreement (but shorter) when compared with the solar angle defined light periods given in [1,4] of 18 April to 24 August at this latitude (79 °N).

Seasonal amplitudes of ambient irradiance are highly dynamic, especially during spring and autumn. The E_{PAR} under a clear sky at noon midsummer, with sun at 30° above horizon (note that Ny-Ålesund maximum is at 22°, Fig. 9), is 300,000 times stronger than an equally high full moon and is estimated to be 30 million times brighter than when both moon and northern lights are absent [4], (Tables 1 and 2). As an estimate of this, taking the maximum E_{PAR} recorded by the camera during our four-year period (305 W m^{-2}, 2019), and the minimum value (0.89×10^{-6} W m^{-2}, 2019), the maximum value is ≈343 million times brighter.

To illustrate the annual E_{PAR} dynamics and daily amplitudes, Fig. 11 shows the daily maximum and minimum values. Additionally, the blue line shows the ratio of daily maximum to minimum recorded values, i.e., the daily variation of E_{PAR} amplitude. It can be clearly seen that during the Midnight Sun and Polar Night periods, the daily maximum and minimum irradiance (amplitude) typically differs by a factor of ≈8. The average ratio observed on the summer solstice over the four-year period was 7.08 while the average ratio for the winter solstice, without a full moon, was 6.49. In contrast, the daily amplitude of E_{PAR} during spring and autumn is in the range of $1-120 \times 10^6$—a period that will act as an important cue for biological processes such as photosynthesis and DVM of zooplankton, and the effects of light pollution during low-light periods [6,14,15].

During low-light periods, the E_{PAR} from the full moon induces a rise in E_{PAR}. However, cloud cover and other phenomena have a very large effect on E_{PAR} during the Polar Night. For example, on 3 December 2017, there was a full moon and aurora visible in a clear sky in the early hours followed by a period of dense cloud cover and visible light pollution giving a amplitude ratio 23.45, a significant increase in variability compared to a typical 24 h period during the Polar Night.

These relatively stable daily E_{PAR} amplitudes during the Midnight Sun and Polar Night periods are in stark contrast to the E_{PAR} dynamics of the transition periods from the end of January to April and the end of August to November, where the daily differences between the maximum and minimum E_{PAR} is on the order of several million. The average value for maximum to minimum ratio of daily E_{PAR} for the spring equinox was 5.3 million, while the average for the autumn equinox was 8.5 million.

5. CONCLUSION

This paper presents a methodology using a camera setup with high light sensitivity and dynamic range to provide images of the atmospheric light regime dynamics and corresponding E_{PAR} in the Arctic. The high dynamic range of the camera allows us to record valid information about the light climate throughout the entire year, especially during the darkest time of the Polar Night. A principal benefit of the all-sky camera approach, over and above increased dynamic range compared with a spectroradiometer, is the ability to capture all-sky images directly showing the conditions which are being measured in an intuitive and easily interpretable manner. Figure 5 shows a series of such images which aid in the quality assessment and interpretation of E_{PAR} and $E(\lambda)$ measurements in a way that is not possible with a more traditional radiometric instrument.

The collected data presented here provides the first year-round time-series recordings of light climate (E_{PAR}, $E(\lambda)$, and photoperiod) with high temporal resolution (e.g., hourly) from the high Arctic, with special attention paid to the low-light season of the Polar Night. The extent to which the Polar Night is affected by moon phases, especially in the period when the sun is

below the horizon all day for several months in the high Arctic, at 79°N in NW-Spitsbergen, has been clearly demonstrated.

This data set is an important step towards documentation of the light climate and how to understand light as a cue to life in the Arctic. The project also provides useful data for light climate modeling and for studies of light as a cue for the dynamics of biological processes and ecosystem functions which are important for terrestrial (including human), limnic, and marine organisms in the Arctic. As mentioned previously, the light climate is comprised of three main components, and further studies are being undertaken to outline the methods of collection and analysis, as well as the uses of spectral data and photoperiod data from the observatory. The results might be important to providing new knowledge concerning the coupling mechanisms between physics and the biological components of Arctic ecosystems. Research of these physical components is crucial for understanding the implications of climate change and guiding environmental policies, i.e., climate-induced changes in albedo, light pollution from human activities, and sea-ice thickness and distribution in polar environments.

In future work, the other aspects of light climate can be explored in addition to highlighting uses of the data and its impacts on a number of key areas including photosynthetic responses, respiration, behavior (e.g., DVM), occurrence and timing of biological processes (e.g., phytoplankton blooms), reproduction, development, and growth as well as modeling the underwater light regime and aligning biological RGB photoreceptors in organisms [25], with the corresponding RGB-derived irradiance data from camera or spectral irradiance to study gene expression and molecule production, among others. A recent publication by Hobbs and colleagues [26], elucidating how marine zooplankton communities are vertically structured by light across diel to inter-annual timescales, pinpointed that zooplankton responses are clearly sensitive to high variation of daily E_{PAR} amplitudes (maximum to minimum ratios) around the spring and autumn equinoxes. This variation in light levels is demonstrated in our findings and indicates that combined studies may be interesting for further understanding and for light-induced modeling of plankton and fish dynamics. The potential applications for the light data presented are broad and can provide much needed light climate data in an ecosystem shrouded in darkness.

Funding. Norges Forskningsråd (223254, 245923, 276730, 300333); Natural Environment Research Council (NE/P00573X/1).

Acknowledgment. We would like to thank the Norwegian Polar Institute and Kings Bay in Ny Ålesund for logistical help. Thanks also to Pedro De La Torre and Sturla Haltbakk (NTNU) for help building the ArcLight observatory.

Disclosures. The authors declare no conflicts of interest.

Data Availability. All data used in the present study will be fully Open Access through NIRD (National Infrastructure for Research Data). The data are published in datasets covering annual time series (2017-2020) from spectroradiometer (raw data and E_{PAR} data, [27–34]) and from all-sky camera (images and E_{PAR} data, [35–42]).

REFERENCES

1. J. H. Cohen, J. Berge, M. A. Moline, G. Johnsen, and A. P. Zolich, "Light in the polar night," in *POLAR NIGHT Marine Ecology—Life and Light in the Dead of the Night*, J. Berge, G. Johnsen, and J. H. Cohen, eds. (Springer, 2020), Chap. 3.
2. E. Sakshaug, G. Johnsen, and Z. Volent, "Light," in *Ecosystem Barents Sea*, E. Sakshaug, G. Johnsen, and K. Kovacs, eds. (Academic, 2009), Chap. 5.
3. J. Berge, G. Johnsen, and J. H. Cohen, "Introduction," in *POLAR NIGHT Marine Ecology—Life and Light in the Dead of the Night*, J. Berge, G. Johnsen, and J. H. Cohen, eds. (Springer, 2020), Chap. 1.
4. Norwegian Hydrographic Service, The Norwegian Pilot: Sailing Directions, Svalbard and Jan Mayen, PDF-version 3.9, 3rd ed. (2018), Vol. **7** https://www.kartverket.no/dnl/den-norske-los-7-english.pdf.
5. J. Berge, M. Daase, P. E. Renaud, W. G. Ambrose, G. Darnis, K. S. Last, E. Leu, J. H. Cohen, G. Johnsen, M. A. Moline, F. Cottier, Ø. Varpe, N. Shunatova, P. Bałazy, N. Morata, J.-C. Massabuau, S. Falk-Petersen, K. Kosobokova, C. J. Hoppe, J. M. Weslawski, P. Kukliński, J. Legeżyńska, D. Nikishina, M. Cusa, M. Kendra, M. W. Kowalczuk, D. Vogedes, L. Camus, D. Tran, E. Michaud, T. M. Gabrielsen, A. Granovitch, A. Gonchar, R. Krapp, and T. A. Callesen, "Unexpected levels of biological activity during the polar night offer new perspectives on a warming arctic," Curr. Biol. **25**, 2555–2561 (2015).
6. J. Berge, G. Johnsen, and J. H. Cohen, *POLAR NIGHT Marine Ecology—Life and Light in The Dead of the Night*, J. Berge, G. Johnsen, and J. H. Cohen, eds. (Springer, 2020).
7. K. Last, L. Hobbs, J. Berge, A. Brierley, and F. Cottier, "Moonlight drives ocean-scale mass vertical migration of zooplankton during the arctic winter," Curr. Biol. **26**, 244–251 (2016).
8. J. H. Cohen, J. Berge, M. A. Moline, A. J. Sørensen, K. Last, S. Falk-Petersen, P. E. Renaud, E. S. Leu, J. Grenvald, F. Cottier, H. Cronin, S. Menze, P. Norgren, Ø. Varpe, M. Daase, G. Darnis, and G. Johnsen, "Is ambient light during the high arctic polar night sufficient to act as a visual cue for zooplankton?" PLoS ONE **10**, 1–12 (2015).
9. H. A. Cronin, J. H. Cohen, J. Berge, G. Johnsen, and M. A. Moline, "Bioluminescence as an ecological factor during high Arctic polar night," Sci. Rep. **6**, 36374 (2016).
10. G. Johnsen, M. Candeloro, J. Berge, and M. A. Moline, "Glowing in the dark: discriminating patterns of bioluminescence from different taxa during the Arctic polar night," Polar Biol. **37**, 707–713 (2014).
11. J. Berge, M. Daase, L. Hobbs, S. Falk-Petersen, G. Darnis, and J. Søreide, "Zooplankton in the polar night," in *POLAR NIGHT Marine Ecology—Life and Light in the Dead of the Night*, J. Berge, G. Johnsen, and J. H. Cohen, eds. (Springer, 2020), Chap. 5.
12. G. Johnsen, E. Leu, and R. Gradinger, "Marine micro- and macroalgae in the polar night," in *POLAR NIGHT Marine Ecology—Life and Light in the Dead of the Night*, J. Berge, G. Johnsen, and J. H. Cohen, eds. (Springer, 2020), Chap. 4.
13. J. Berge, P. Renaud, G. Darnis, F. Cottier, K. Last, T. M. Gabrielsen, G. Johnsen, L. Seuthe, J. M. Weslawski, E. Leu, M. A. Moline, J. Nahrgang, J. Søreide, Ø. Varpe, O. J. Lønne, M. Daase, and S. Falk-Petersen, "In the dark: a review of ecosystem processes during the Arctic polar night," Prog. Oceanograph. **139**, 258–271 (2015b).
14. M. Ludvigsen, J. Berge, M. Geoffroy, J. H. Cohen, P. R. De La Torre, S. M. Nornes, H. Singh, A. J. Sørensen, M. Daase, and G. Johnsen, "Use of an autonomous surface vehicle reveals small-scale diel vertical migrations of zooplankton and susceptibility to light pollution under low solar irradiance," Sci. Adv. **4**, eaap9887 (2018).
15. J. Berge, M. Geoffroy, M. Daase, F. Cottier, P. Priou, J. H. Cohen, G. Johnsen, D. McKee, I. Kostakis, P. E. Renaud, D. Vogedes, P. Anderson, K. Last, and S. Gauthier, "Artificial light during the polar night disrupts Arctic fish and zooplankton behaviour down to 200 m depth," Commun. Biol. **3**, 102 (2020).
16. "Amendment 1, Part 2-1, Colour management - default RGB colour space - sRGB," International standard IEC 61966-2-1, IEC, 2003, available at https://www.sis.se/std-562720. This annex provides equations necessary for extended gamut encoding for sRGB.
17. "Photography—General purpose photographic exposure meters (photoelectric type)—Guide to product specification," ISO 270:1974 (ISO, 1974).
18. S. H. Baek, I. Kim, D. Guitierrez, and M. H. Kim, "Compact single-shot hyperspectral imaging using a prism," ACM Trans. Graph. **36**, 217 (2017).

19. P. D. Hiscocks, "Measuring luminance with a digital camera," 2011,https://www.semanticscholar.org/paper/Measuring-Luminance-with-a-Digital-Camera-Hiscocks-Syscomp/a541a601bf3ce56f8f4f6264374c2c5349dc09bb.
20. E. Sakshaug, G. Johnsen, and K. Kovacs, eds. *Ecosystem Barents Sea* (Academic, 2009), Provides approximate conversion factors of irradiance (400-700 nm) from W m−2 to μmol photons m−2 s−1.
21. A. K. Pavlov, E. Leu, D. Hanelt, I. Bartsch, U. Karsten, S. R. Hudson, J. C. Gallet, F. Cottier, J. H. Cohen, J. Berge, G. Johnsen, M. Maturilli, P. Kowalczuk, S. Sagan, J. Meler, and M. A. Granskog, "The underwater light climate in Kongsfjorden and its ecological implications," in *The Ecosystem of Kongsfjorden, Svalbard, Advances in Polar Ecology*, H. Hop and C. Wiencke, eds. (Springer, 2019), Vol. **2**.
22. K. Hancke, L. C. Lund-Hansen, M. L. Lamare, S. H. Pedersen, M. D. King, P. Andersen, and B. K. Sorrell, "Extreme low light requirements for algae growth underneath sea ice: a case study from Station Nord, NE Greenland," J. Geophys. Res. Oceans **123**, 985–1000 (2018).
23. G. Johnsen, E. Sakshaug, and M. Vernet, "Pigment composition, spectral characterization and photosynthetic parameters in *Chrysochromulina polylepis*," Mar. Ecol. Prog. Ser. **83**, 241–249 (1992).
24. G. Johnsen and E. Sakshaug, "Bio-optical characteristics of PSII and PSI in 33 species (13 pigment groups) of marine phytoplankton, and the relevance for PAM and FRR fluorometry," J. Phycol. **43**, 1236–1251 (2007).
25. K. C. Valle, M. Nymark, I. Aamot, K. Hancke, P. Winge, K. Andresen, G. Johnsen, T. Brembu, and A. Bones, "System responses to equal doses of photosynthetically usable radiation of blue, green, and red light in the marine diatom *Phaeodactylum tricornutum*," PLoS ONE **9**, e114211 (2014).
26. L. Hobbs, N. S. Banas, J. H. Cohen, F. R. Cottier, J. Berge, and Ø. Varpe, "A marine zooplankton community vertically structured by light across diel to interannual timescales," Biol. Lett. **17**, 20200810 (2021).
27. J. Berge, S. Grant, R. Bjørgum, J. H. Cohen, D. McKee, G. Johnsen, A. Zolich, T. P. Kopec, and D. L. Vogedes, *USSIMO Spectroradiometer Raw Data Time Series (2018) Measured under the Dome of a Light Observatory in the Arctic (Ny-Ålesund, Svalbard, Norway) [Data Set]* (Norstore, 2021).
28. J. Berge, S. Grant, R. Bjørgum, J. H. Cohen, D. McKee, G. Johnsen, A. Zolich, T. P. Kopec, and D. L. Vogedes, *USSIMO Spectroradiometer Raw Data Time Series (2019) Measured under the Dome of a Light Observatory in the Arctic (Ny-Ålesund, Svalbard, Norway) [Data Set]* (Norstore, 2021).
29. J. Berge, S. Grant, R. Bjørgum, J. H. Cohen, D. McKee, G. Johnsen, A. Zolich, T. P. Kopec, and D. L. Vogedes, *USSIMO Spectroradiometer Raw Data Time Series (2020) Measured under the Dome of a Light Observatory in the Arctic (Ny-Ålesund, Svalbard, Norway) [Data Set]* (Norstore, 2021).
30. J. Berge, S. Grant, R. Bjørgum, J. H. Cohen, D. McKee, G. Johnsen, A. Zolich, T. P. Kopec, and D. L. Vogedes, *USSIMO Spectroradiometer Raw Data Time Series (2017) Measured under the Dome of a Light Observatory in the Arctic (Ny-Ålesund, Svalbard, Norway) [Data Set]* (Norstore, 2021).
31. J. Berge, S. Grant, R. Bjørgum, J. H. Cohen, D. McKee, G. Johnsen, A. Zolich, T. P. Kopec, and D. L. Vogedes, *Time Series (2020) of Irradiance in the PAR (Photosynthetic Active Radiation) Measured under the Dome of a Light Observatory in the Arctic (Ny-Ålesund, Svalbard, Norway) Derived from an USSIMO Spectroradiometer. [Data Set]* (Norstore, 2021).
32. J. Berge, S. Grant, R. Bjørgum, J. H. Cohen, D. McKee, G. Johnsen, A. Zolich, T. P. Kopec, and D. L. Vogedes, *Time Series (2019) of Irradiance in the PAR (Photosynthetic Active Radiation) Measured under the Dome of a Light Observatory in the Arctic (Ny-Ålesund, Svalbard, Norway) Derived from an USSIMO Spectroradiometer. [Data Set]* (Norstore, 2021).
33. J. Berge, S. Grant, R. Bjørgum, J. H. Cohen, D. McKee, G. Johnsen, A. Zolich, T. P. Kopec, and D. L. Vogedes, *Time Series (2018) of Irradiance in the PAR (Photosynthetic Active Radiation) Measured under the Dome of a Light Observatory in the Arctic (Ny-Ålesund, Svalbard, Norway) Derived from an USSIMO Spectroradiometer. [Data Set].* (Norstore, 2021).
34. J. Berge, S. Grant, R. Bjørgum, J. H. Cohen, D. McKee, G. Johnsen, A. Zolich, T. P. Kopec, and D. L. Vogedes, *Time Series (2017) of Irradiance in the PAR (Photosynthetic Active Radiation) Measured under the Dome of a Light Observatory in the Arctic (Ny-Ålesund, Svalbard, Norway) Derived from an USSIMO Spectroradiometer. [Data Set].* (Norstore, 2021).
35. G. Johnsen, S. Grant, R. Bjørgum, J. H. Cohen, D. McKee, T. P. Kopec, D. L. Vogedes, J. Berge, and A. Zolich, *Pictures from an All-Sky Camera with Hourly Resolution from the Light Observatory at Ny-Ålesund, Svalbard, Norway (Complete Year 2017) [Data Set]* (Norstore, 2021).
36. G. Johnsen, S. Grant, R. Bjørgum, J. H. Cohen, D. McKee, T. P. Kopec, D. L. Vogedes, J. Berge, and A. Zolich, *Pictures from an All-Sky Camera with Hourly Resolution from the Light Observatory at Ny-Ålesund, Svalbard, Norway (Complete Year 2018) [Data Set]* (Norstore, 2021).
37. G. Johnsen, S. Grant, R. Bjørgum, J. H. Cohen, D. McKee, T. P. Kopec, D. L. Vogedes, J. Berge, and A. Zolich, *Pictures from an All-Sky Camera with Hourly Resolution from the Light Observatory at Ny-Ålesund, Svalbard, Norway (Complete Year 2019) [Data Set]* (Norstore, 2021).
38. G. Johnsen, S. Grant, R. Bjørgum, J. H. Cohen, D. McKee, T. P. Kopec, D. L. Vogedes, J. Berge, and A. Zolich, *Pictures from an All-Sky Camera with Hourly Resolution from the Light Observatory at Ny-Ålesund, Svalbard, Norway (Complete Year 2020) [Data Set]* (Norstore, 2021).
39. G. Johnsen, S. Grant, R. Bjørgum, J. H. Cohen, D. McKee, T. P. Kopec, D. L. Vogedes, J. Berge, and A. Zolich, *Time Series (2017) of Irradiance in the PAR (Photosynthetically Active Radiation) Region Measured under the Dome of a Light Observatory in the Arctic (Ny-Ålesund, Svalbard, Norway) Derived from SLR Camera [Data Set]* (Norstore, 2021).
40. G. Johnsen, S. Grant, R. Bjørgum, J. H. Cohen, D. McKee, T. P. Kopec, D. L. Vogedes, J. Berge, and A. Zolich, *Time Series (2018) of Irradiance in the PAR (Photosynthetically Active Radiation) Region Measured under the Dome of a Light Observatory in the Arctic (Ny-Ålesund, Svalbard, Norway) Derived from SLR Camera [Data Set]* (Norstore, 2021).
41. G. Johnsen, S. Grant, R. Bjørgum, J. H. Cohen, D. McKee, T. P. Kopec, D. L. Vogedes, J. Berge, and A. Zolich, *Time Series (2019) of Irradiance in the PAR (Photosynthetically Active Radiation) Region Measured under the Dome of a Light Observatory in the Arctic (Ny-Ålesund, Svalbard, Norway) Derived from SLR Camera [Data Set]* (Norstore, 2021).
42. G. Johnsen, S. Grant, R. Bjørgum, J. H. Cohen, D. McKee, T. P. Kopec, D. L. Vogedes, J. Berge, and A. Zolich, *Time series (2020) of Irradiance in the PAR (Photosynthetically Active Radiation) Region Measured under the Dome of a Light Observatory in the Arctic (Ny-Ålesund, Svalbard, Norway) Derived from SLR Camera [Data Set]* (Norstore, 2021).